

Shifted Frequency Modeling of Hybrid Modular Multilevel Converters for Simulation of MTDC Grid

Dewu Shu ¹, *Student Member, IEEE*, Venkata Dinavahi ², *Senior Member, IEEE*,
Xiaorong Xie ¹, *Senior Member, IEEE*, and Qirong Jiang ¹, *Member, IEEE*

Abstract—When investigating voltage and current stresses in critical main circuit components during faults of the converter, a detailed equivalent model capable of representing the balancing control strategies of the capacitor voltages on the submodule level, along with blocking and delocking, is always necessary. Among previously proposed equivalent models of the modular multilevel converter (MMC), only submodule averaged models (SAMs) can capture interested inner dynamics inside each arm. However, the simulation accuracy of SAMs is not always satisfactory, especially when the time step is larger than 10 μ s. In order to further improve the simulation accuracy with guaranteed simulation efficiency, the shifted frequency modeling of the half- and full-bridge hybrid MMC is proposed in this paper. Therein, each submodule is represented by Thévenin equivalents derived by submodule dynamic phasors. The arm of the MMC is represented by Norton equivalents to guarantee the efficiency, considering both normal and dc-blocking conditions. The effectiveness of the proposed model in terms of accuracy and efficiency is validated by simulating an MMC-based HVdc transmission.

Index Terms—Dynamic phasors, electromagnetic transient (EMT), modular multilevel converter (MMC), MTDC grid, shifted frequency modeling.

I. INTRODUCTION

AS ONE of the most promising multilevel voltage source converters (VSCs), the modular multilevel converter (MMC) offers many merits such as smaller distortions, low switching losses, and smaller filter sizes [1]–[4]. To validate the parameter design and the control scheme of the MMC-based HVDC transmission, it is critical to simulate the MMC in electromagnetic transient (EMT) programs. However, the detailed simulation model of the MMC is inefficient due to the following reasons: 1) the detailed model should use a small numerical

integration time-step to accurately represent fast switching events; 2) the admittance matrix should be updated during every switching event, which will impose a significant computational burden for EMT simulations [5]. In addition, when the MMC is under the dc-fault blocking condition, the IGBTs are all switched off and the dynamic behavior of the MMC can be quite different from normal conditions due to the nonlinear characteristics of freewheeling diodes [6]. Notably, when investigating voltage and current stresses during faults inside or immediately outside the converter, quantities of each individual sub-module must be simulated in detail. Therefore, in order to improve the simulation efficiency without compromising the accuracy, it is still required to propose more accurate and efficient methods of modeling, which is capable of representing inner dynamics of each sub-module as well as the dynamic characteristics of the diodes.

Several models of the MMC have been previously proposed, which are summarized in Table I. Specifically, the analytical models of the MMC are based on mathematical models of the MMC, which are represented in the form of state-space equations [7]–[9]. These models are accurate to represent system-level dynamics under normal conditions. However, since the characteristics of the diodes are not taken into consideration in these models, the MMCs in dc-fault blocking conditions cannot be represented accurately. More importantly, the inner dynamics inside each arm, i.e., the specific dynamic characteristics of each sub-module, cannot be represented. The arm-averaged models (AAMs), on the other hand, are developed under the hypothesis that capacitor voltages inside each arm are perfectly balanced, and therefore each arm can be modeled as a Thévenin equivalent circuit [5], a controlled voltage source [14], etc., accompanied by a series of diodes or switches [18]. In [11], an AAM with a controlled voltage source model was proposed to represent the half-bridge sub-module based MMC under blocking conditions. However, the equivalent arm circuits adopting other types of sub-modules were not comprehensively analyzed. Recently, the dynamic phasor model of the MMC was derived in the form of state-space equations [16], [17]. However, as no diode is represented in this model, it can only be used to simulate dynamics under normal conditions, and dc-blocking conditions are omitted. Moreover, from Table I, only submodule averaged models (SAMs) can capture the inner dynamics inside each arm, while other models, such as analytical models and AAMs fail at this task. Although the simulation efficiency has been improved by SAMs, the accuracy is not always satisfactory, especially when the time-step is larger than 10 μ s.

Manuscript received April 25, 2017; revised June 26, 2017 and August 21, 2017; accepted September 2, 2017. Date of publication September 6, 2017; date of current version April 6, 2018. This work was supported in part by the National Key Research and Development Program of China under Grant 2017YFB0902002, in part by the Natural Sciences and Engineering Research Council of Canada, and in part by the National Natural Science Foundation of China (51737007). Paper no. TPWRD-00582-2017. (*Corresponding author: Xiaorong Xie.*)

D. Shu, X. Xie, and Q. Jiang are with the State Key Laboratory of Power System, Department of Electrical Engineering, Tsinghua University, Beijing 100084, China (e-mail: shudw13@mails.tsinghua.edu.cn; xiexr@tsinghua.edu.cn; qrjiang@tsinghua.edu.cn).

V. Dinavahi is with the Department of Electrical and Computer Engineering, University of Alberta, Edmonton, AB T6G1H9, Canada (e-mail: dinavahi@ualberta.ca).

Color versions of one or more of the figures in this paper are available online at <http://ieeexplore.ieee.org>.

Digital Object Identifier 10.1109/TPWRD.2017.2749427

TABLE I
COMPARISON OF DIFFERENT MODELING METHODS OF THE MMCs

	Methods	Dynamics of Interest	Efficiency
Analytical Models	steady-state model [7] continuous-variable dynamic model [8], [9]	System-level steady state (to validate the parameter design)	Most efficient
Arm averaged models (AAMs)	Thévenin equivalent model [5]	System-level dynamics under normal condition System-level dynamics between the MMCs and AC grid; capacitor voltages inside each arm are assumed perfectly balanced	Very efficient
Sub-module averaged models (SAMs)	Controlled voltage model [10] Switch function model [11] Continuous model [12], [13]	System-level dynamics between the MMCs and AC grid; inner dynamics inside each arm	Less efficient
Dynamic phasor model	Thévenin equivalent model [5] Controlled voltage model [14], [15] Switch function model [6] State space based dynamics phasor model [16], [17]	System-level dynamic under normal conditions; dc-fault blocking condition cannot simulated	Very efficient

In order to further improve the simulation accuracy with guaranteed efficiency, the shifted frequency modeling (SFM) of the MMC is proposed in this paper, where the circuit configuration of the hybrid MMC is a mixture of half-bridge sub-modules (HBSMs) and full-bridge sub-modules (FBSMs). Its salient features include:

- 1) The SFM based MMC model has improved accuracy than the traditional SAMs. This is due to the Thévenin equivalent circuit derived by SFM is more accurate than the traditional Trapezoidal-derived models.
- 2) The arm model of the MMC is represented by one Norton equivalent circuit, considering both normal and dc-blocking conditions. As the number of nodes will not expand as the number of sub-modules increases, the simulation efficiency is guaranteed.

The rest of the paper is organized as follows: Section II introduces the principle of shifted frequency analysis (SFA); Section III gives the SFM of the half-bridge and full bridge MMCs, including the equivalent model of half-bridge and full-bridge sub-modules and the corresponding equivalent arm model. In Section IV, a MMC-based HVDC transmission is used to prove the effectiveness of the SFM for the MMC. Section V draw the conclusions.

II. SHIFTED FREQUENCY ANALYSIS

A. Brief Introduction

A signal in power system (see Fig. 1, which typically has a spectrum centered at the fundamental frequency ω_s , can be characterized as [19], [20]

$$s(t) = \lim_{\Delta\omega \rightarrow 0} \sum_{i=-\infty}^{\infty} a_i \cos [(\omega_s + i\Delta\omega)t + \phi_i], \quad (1)$$

where $\Delta\omega$ is the frequency band around ω_s . Using a trigonometric formula, (1) can be reformulated as

$$s(t) = s_I(t) \cos \omega_s t - s_Q(t) \sin \omega_s t, \quad (2)$$

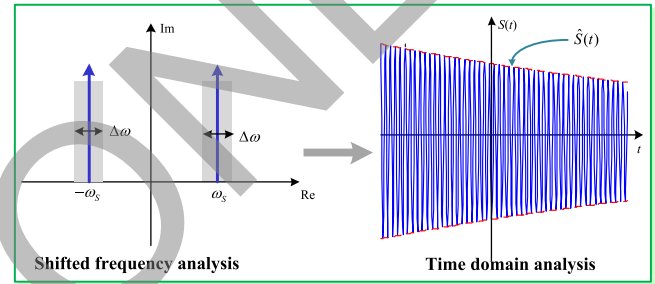


Fig. 1. Concept of shifted frequency analysis.

where

$$\begin{cases} s_I(t) = \lim_{\Delta\omega \rightarrow 0} \sum_{i=-\infty}^{\infty} a_i \cos [i\Delta\omega t + \phi_i], \\ s_Q(t) = \lim_{\Delta\omega \rightarrow 0} \sum_{i=-\infty}^{\infty} a_i \sin [i\Delta\omega t + \phi_i], \end{cases} \quad (3)$$

Since $s_I(t)$ and $s_Q(t)$ contains all the information about the bandpass signal $s(t)$, one possible way of representing the real signal $s(t)$ is by the means of its dynamic phasor form:

$$\begin{cases} S(t) = \hat{S}(t)e^{j\omega_s t} \\ \hat{S}(t) = s_I(t) + js_Q(t), \end{cases} \quad (4)$$

$\hat{S}(t)$ is also called complex envelope of the time-domain signal $s(t)$, which preserves the low frequency dynamics of $s(t)$ around ω_s . As a result, the above-mentioned representations of signals are named as the ‘‘shifted frequency’’ representations.

Equation (4) can be also expressed as follows [21]–[23]:

$$S(t) = s(t) + jH[s(t)], \quad (5)$$

where

$$H[s(t)] = \frac{1}{\pi} \int_{-\infty}^{\infty} \frac{s(\tau)}{t - \tau} d\tau \quad (6)$$

denotes the Hilbert transformation.

From the above derivations, it can be concluded that the shifted frequency representation of each power system component can be achieved by either mathematical properties of

dynamic phasors, i.e., the product and the differential features of dynamic phasors [24]–[26] or the Hilbert transformation.

To demonstrate the application of the SFA in EMT simulations, the capacitor is used as an illustrate example. Represented in the dynamic phasor form, the differential equation of the capacitor is given as [27], [28]:

$$\widehat{i}_C(t) = C \frac{d\widehat{v}_C(t)}{dt} + j\omega_s C \widehat{v}_C(t), \quad (7)$$

where $\widehat{i}_C(t)$, $\widehat{v}_C(t)$ denotes the capacitor current and voltage in the dynamic phasor form.

According to the derivation of SFM given in Appendix A, the Norton equivalents, i.e., the conductance matrix as well as the equivalent current vector, are written with separate real and imaginary parts as:

$$\begin{cases} \begin{bmatrix} i_{cx}(t) \\ i_{cy}(t) \end{bmatrix} = G_{cxy} \begin{bmatrix} v_{cx}(t) \\ v_{cy}(t) \end{bmatrix} + \begin{bmatrix} J_{cx}(t - \Delta t) \\ J_{cy}(t - \Delta t) \end{bmatrix}, \\ \begin{bmatrix} J_{cx}(t - \Delta t) \\ J_{cy}(t - \Delta t) \end{bmatrix} = K_v \begin{bmatrix} v_{cx}(t - \Delta t) \\ v_{cy}(t - \Delta t) \end{bmatrix} + K_i \begin{bmatrix} i_{cx}(t - \Delta t) \\ i_{cy}(t - \Delta t) \end{bmatrix}, \end{cases} \quad (8)$$

satisfying:

$$\begin{cases} G_{cxy} = \frac{2C}{\Delta t} I_{2 \times 2} - \mathbf{R} \left(-\frac{\pi}{2\omega_s} \right) \omega_s C, \\ K_v = -\frac{2C}{\Delta t} I_{2 \times 2} - \mathbf{R} \left(-\frac{\pi}{2\omega_s} \right) \omega_s C, \text{ and} \\ K_i = -\mathbf{R} \left(-\frac{\pi}{2\omega_s} \right), \end{cases} \quad (9)$$

where

$$\mathbf{R}(t) = \begin{bmatrix} \cos \omega_s t & \sin \omega_s t \\ -\sin \omega_s t & \cos \omega_s t \end{bmatrix}. \quad (10)$$

And G_{cxy} , $[J_{cx}, J_{cy}]^T$ denotes the conductance matrix and the equivalent current vector in xy coordinates (x/y denotes real /imaginary parts, respectively). Hence, (8), (9) constitutes the Norton equivalents of the capacitor by SFA. Moreover, the corresponding Thévenin equivalents are written as:

$$\begin{cases} Z_{cxy} = [G_{cxy}]^{-1} \\ v_{cxy} = -[G_{cxy}]^{-1} [J_{cx}(t - \Delta t) \quad J_{cy}(t - \Delta t)]^T \end{cases} \quad (11)$$

where Z_{cxy} is impedance matrix and v_{cxy} is the equivalent voltage vector.

Thus, modeling of each power system component by SFA includes the following three steps:

- 1) Obtain the time-domain differential equation of the model and transform the equation into the dynamic phasor form;
- 2) Discretize the differential equation in the dynamic phasor form and transform it into the form of time-domain signals;
- 3) The equation in the time-domain is rewritten with separate real and imaginary parts. Finally, the Norton equivalent matrix in the xy -coordinates is derived.

Unlike the traditional time-domain EMT analysis [29], [30], the fast time-varying signals are converted into slow time-varying dynamic phasors by the SFA. Low frequency dynamic

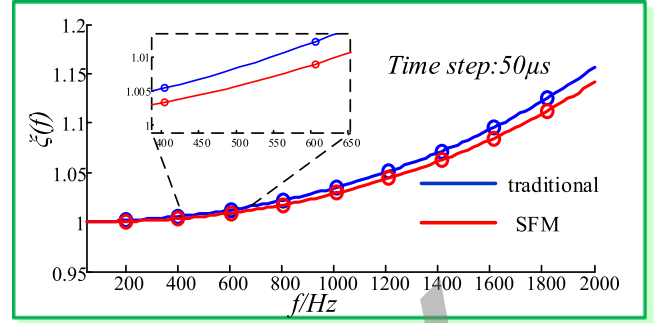


Fig. 2. Ratio of conductance for the SFM and the traditional model.

phasors imply the feasibility of using larger integration time steps. Therefore, the calculation burden of the SFA can be significantly reduced, and the simulation efficiency can be improved greatly.

B. Accuracy Comparisons Between SFM and Traditional Methods

To compare the accuracy of SFM and the Trapezoidal algorithm, which is adopted by the traditional EMT time-domain analysis, the model of the capacitor is used again. The ratio of the admittance derived by numerical algorithms and its actual value, defined in (12), is used as a measure of accuracy:

$$\xi(f) = Y^n(2\pi f) / Y^a(2\pi f), \quad (12)$$

where $Y^n(2\pi f)$ is the conductance obtained with the different numerical algorithms; $Y^a(2\pi f)$ is the actual conductance.

According to [31], [32], the difference equation for the capacitor by the trapezoidal algorithm is given as:

$$v_C(t) - v_C(t - \Delta t) = \frac{\Delta t}{2C} [i_C(t) + i_C(t - \Delta t)]. \quad (13)$$

Equation (13) is converted into the z -domain as:

$$Y_T^n(z) = \frac{i_C(z)}{v_C(z)} = \frac{2C}{\Delta t} \frac{1 - z^{-1}}{1 + z^{-1}}, \quad (14)$$

where $z = e^{j2\pi f \Delta t}$. So the conductance can be numerically calculated, as in (14), and then the ratio of conductances is obtained:

$$\xi_T(f) = Y_T^n(z) / Y^a(2\pi f) = \frac{\tan(2\pi f \Delta t / 2)}{2\pi f \Delta t / 2}. \quad (15)$$

According to (8), (9), the ratio of conductance by SFM is derived as [27]:

$$\begin{aligned} \xi_S(f) &= Y_T^n(z) / Y^a(2\pi f) = \frac{\frac{2}{\Delta t} \tan\left(\frac{(\omega - \omega_s)\Delta t}{2}\right) + \omega_s}{\omega}, \\ \omega &= 2\pi f. \end{aligned} \quad (16)$$

According to its definition, the closer $\xi(f)$ is to the unity, the more precise the algorithm becomes. It can be observed from Fig. 2 that the SFM method has better accuracy than the traditional Trapezoidal-derived method within the whole frequency range, i.e., [60 Hz, 2000 Hz]. The relative accuracy improvement of the SFM compared with the traditional model,

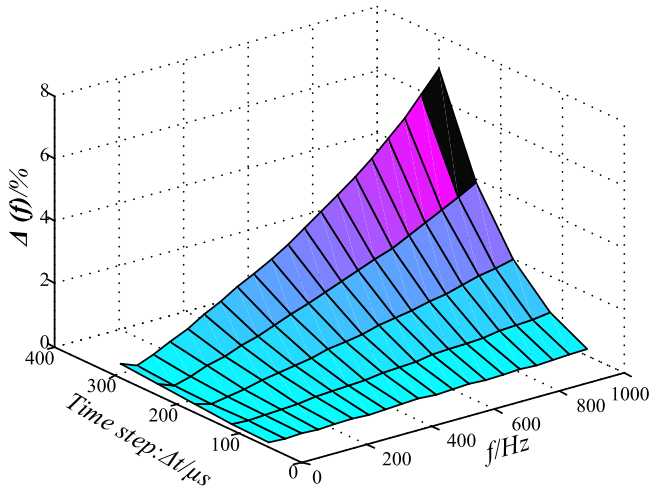


Fig. 3. Accuracy improvement of SFM compared with the traditional model.

i.e., $\Delta(f) = |(\xi_S(f) - \xi_T(f))/\xi_T(f)| \times 100\%$ is shown in Fig. 3. As can be seen, the accuracy improvement of SFM increases as the time step/frequency rises. Specifically, at the time step of $50 \mu s$, the SFM method achieves a more than 2% increase of accuracy when the frequency is higher than 1 kHz.

III. SHIFTED FREQUENCY MODELING OF THE HYBRID MODULAR MULTI-LEVEL CONVERTER

Due to the small number of devices and low investment cost, the half-bridge sub-module (HBSM) is widely used for industrial applications. However, this topology can produce large DC fault currents, which bring challenges for the protection of the MMCs. This problem can be overcome by using additional full-bridge sub-modules (FBSMs), as it can produce both positive and negative voltages and preserves the DC fault ride-through capability. Combining the advantages of HBSM and FBSM, each arm of the MMC converter is mixed with the unipolar HBSM and the bipolar FBSM to form the half- and full-bridge MMC, which is shown in Fig. 4. Specifically, each arm has H HBSMs (HBSM₁ to HBSM_H) and F FBSMs (FBSM₁ to FBSM_F). L_u and L_d is the arm inductance of upper and lower arm, respectively.

Traditionally, the shifted frequency analysis has been used for the modeling of generators [21], [22], RLC circuits [27], [28], and frequency dependent transmission lines [33]. Different from conventional components in power systems, the SFM of the MMC encounters the following special challenges:

- 1) Instead of the single conductance or the equivalent current terms, each component by SFA is represented by the derived conductance matrix as well as the equivalent current vector, covering both the real and imaginary parts;
- 2) There may exist couplings between the real and imaginary parts of the nodal conductance matrix, which make the determination of switch-on/off time of power electronic switches more complicated. Therefore, resolving the numerical oscillations aroused by switching is a formidable challenge for the SFA than the traditional one;

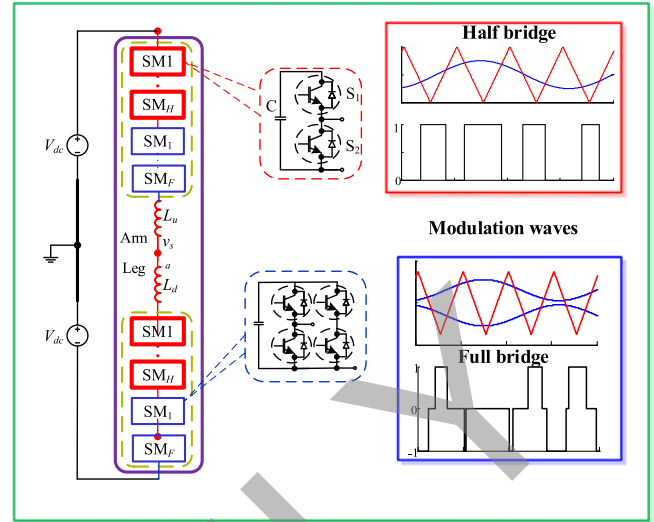


Fig. 4. Structure of the half- and full-bridge sub-modules in the MMC.

- 3) During each iteration of the simulation, it is necessary to update the real and imaginary parts of all the variables in each sub-module simultaneously.

In the following, the SFM of the half- and full-bridge MMC is proposed to resolve the above challenges. Specifically, Section III-A details the equivalent model of each sub-module with half-bridge or full-bridge topologies; the arm equivalent model is finally derived in Section III-B.

A. Equivalent Models of Half-Bridge and Full Bridge Sub-Modules

In order to resolve the second challenge, i.e., avoid the numerical oscillations caused by switching and improve the simulation efficiency, the Thévenin equivalent model, represented by SFM, is used for each sub-module. Since the equivalent model has no switch inside, naturally there is no risk of numerical oscillation [29], [30].

For each sub-module, regardless of the HBSM or the FBSM topology, the capacitor voltages need to be updated only when the corresponding sub-module is operated; otherwise, the capacitor voltages can remain unchanged. According to (8), (9), the updated equation for capacitor voltages are derived as

$$\begin{bmatrix} v_{cx}(t) \\ v_{cy}(t) \end{bmatrix} = [G_{cxy}]^{-1} \left\{ \begin{bmatrix} i_{cx}(t) \\ i_{cy}(t) \end{bmatrix} - K_v \begin{bmatrix} v_{cx}(t - \Delta t) \\ v_{cy}(t - \Delta t) \end{bmatrix} - K_i \begin{bmatrix} i_{cx}(t - \Delta t) \\ i_{cy}(t - \Delta t) \end{bmatrix} \right\}. \quad (17)$$

The voltage drop on the switches in HBSM is expressed as [6]:

$$v_h(t) = \begin{cases} R_d \cdot i_{arm}(t) + V_d, i_{arm}(t) > 0 \text{ and } S_h(t) = 1, \\ R_i \cdot i_{arm}(t) - V_d, i_{arm}(t) < 0 \text{ and } S_h(t) = 1, \\ R_i \cdot i_{arm}(t) + V_d, i_{arm}(t) > 0 \text{ and } S_h(t) = 0, \\ R_d \cdot i_{arm}(t) - V_d, i_{arm}(t) < 0 \text{ and } S_h(t) = 0, \end{cases} \quad (18)$$

where $i_{arm}(t)$ denotes the arm current; $S_h(t)$ is the switch function of the HBSM; R_d , R_i are the on-state resistances of diode and IGBT, respectively; V_d , V_i are the corresponding on-state threshold voltages.

The voltage drop on the switches in HBSM in xy coordinates is written as $[v_{hx}(t) \ v_{hy}(t)]^T = v_h(t) \cdot I_{2 \times 2}$. Moreover, the equivalent impedance matrix corresponding to the power electronic devices for HBSM is written as:

$$Z_h(t) = \begin{cases} R_d, i_{arm}(t) > 0 \text{ and } S_h(t) = 1, \\ R_i, i_{arm}(t) < 0 \text{ and } S_h(t) = 1, \\ R_i, i_{arm}(t) > 0 \text{ and } S_h(t) = 0, \\ R_d, i_{arm}(t) < 0 \text{ and } S_h(t) = 0, \end{cases} \quad (19)$$

Therefore, the corresponding equivalent impedance matrix in xy coordinates is expressed as:

$$Z_{hxy}(t) = Z_h(t) \cdot \left[I_{2 \times 2} + \mathbf{R} \left(-\frac{\pi}{2\omega_s} \right) \right], \quad (20)$$

where $\mathbf{R}(\cdot)$ is referred to (10).

Similarly, the voltage drop on the switches in FBSM can be derived, i.e., $v_{fxy}(t)$, satisfying $v_{fxy}(t) = [v_{fx}(t) \ v_{fy}(t)]^T = v_f(t) \cdot I_{2 \times 2}$. In xy coordinates, the corresponding equivalent impedance matrix for the power electronic devices for FBSM is given as

$$Z_{fxy}(t) = Z_f(t) \cdot \left[I_{2 \times 2} + \mathbf{R} \left(-\frac{\pi}{2\omega_s} \right) \right] \quad (21)$$

In summary, taking the HBSM as an example, the equivalent impedance matrix $Z_{Hxy}(t)$ and the Thévenin equivalent voltage vector $v_{Hxy}(t)$ of each HBSM are given as follows:

$$Z_{Hxy}(t) = \begin{cases} Z_{hxy}(t) + Z_{cxy}(t), S_h(t) = 1, \\ Z_{hxy}(t), S_h(t) = 0, \end{cases} \quad (22)$$

$$v_{Hxy}(t) = \begin{cases} v_{hxy}(t) + v_{cxy}(t), S_h(t) = 1, \\ v_{hxy}(t), S_h(t) = 0. \end{cases} \quad (23)$$

where $Z_{cxy}(t)$, $v_{cxy}(t)$ are referred to (11); $Z_{hxy}(t)$, $v_{hxy}(t)$ are referred to (18)–(20). Equations (22) and (23) correspond to the proposed SFM-based Thévenin equivalent model of HBSM. The model for the FBSM, i.e., $Z_{fxy}(t)$, $v_{fxy}(t)$, can be similarly derived.

B. Equivalent Arm Model for the Half- and Full-Bridge MMC Converter

As shown in Fig. 4, each arm contains multiple HBSMs and FBSMs, which are connected in series. The final SFM-based Thévenin equivalent model of each arm can be obtained by combining the equivalent models of all the sub-modules. Thus, the equivalent impedance matrix $Z_{xy}^H(t)$ and the Thévenin equivalent voltage vector $v_{xy}^H(t)$ of all the HBSMs is given as:

$$\begin{cases} Z_{xy}^H(t) = \sum_{i=1}^H Z_{Hxy}^i(t), \\ v_{xy}^H(t) = \sum_{i=1}^H v_{Hxy}^i(t), \end{cases} \quad (24)$$

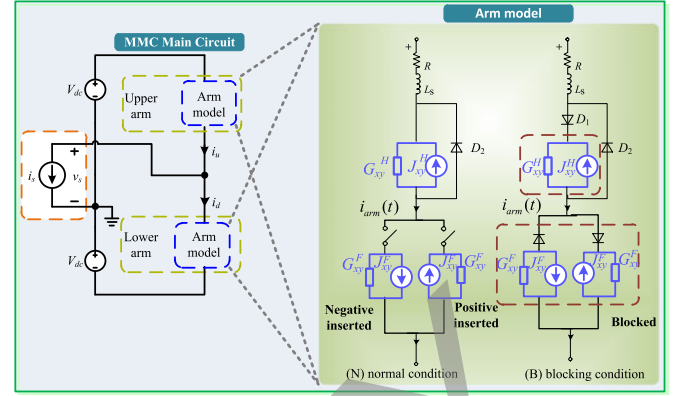


Fig. 5. Equivalent arm model for the half- and full-bridge hybrid MMC when considering the DC-fault blocking capability.

where $Z_{Hxy}^i(t)$, $v_{Hxy}^i(t)$ correspond to the equivalent impedance matrix as well as the Thévenin equivalent voltage vector of i th HBSM; H is the number of the HBSMs in the MMC arm.

Further, the Norton equivalent circuit corresponding to all the HBSMs is derived as:

$$\begin{cases} G_{xy}^H(t) = 1/Z_{xy}^H(t), \\ J_{xy}^H(t) = -v_{xy}^H(t)/Z_{xy}^H(t), \end{cases} \quad (25)$$

where $G_{xy}^H(t)$, $J_{xy}^H(t)$ denotes its conductance matrix and the equivalent current vector.

Similarly, the equivalent impedance matrix and the Thévenin equivalent voltage vector of all the FBSMs are given as:

$$\begin{cases} Z_{xy}^F(t) = \sum_{i=1}^F Z_{Fxy}^i(t), \\ v_{xy}^F(t) = \sum_{i=1}^F v_{Fxy}^i(t), \end{cases} \quad (26)$$

where $Z_{Fxy}^i(t)$, $v_{Fxy}^i(t)$ correspond to the equivalent impedance matrix as well as the Thévenin equivalent voltage vector of i th FBSM; F is the number of the FBSMs in the MMC arm.

Then, the Norton equivalent circuit corresponding to all the FBSMs is derived as:

$$\begin{cases} G_{xy}^F(t) = 1/Z_{xy}^F(t), \\ J_{xy}^F(t) = -v_{xy}^F(t)/Z_{xy}^F(t), \end{cases} \quad (27)$$

where $G_{xy}^F(t)$, $J_{xy}^F(t)$ denotes its conductance matrix and the equivalent current vector.

Finally, the equivalent arm model for the half- and full-bridge MMC converter when considering the DC-fault blocking capability is depicted in Fig. 5. As can be seen, only one node is added in the nodal voltage equation of the system for each phase, otherwise the dimension of the nodal voltage equation will be expanded by $N + 1$ if the SAM models are adopted [34]. Here, N refers to the number of sub-modules. This is why the proposed Norton equivalent circuit guarantees the simulation efficiency by reducing the number of nodes in each arm. Moreover, parameters of each sub-module, i.e., $Z_{Hxy}^i(t)$, $v_{Hxy}^i(t)$, $i = 1, 2, \dots, H$ and $Z_{Fxy}^i(t)$, $v_{Fxy}^i(t)$, $i = 1, 2, \dots, F$, are calculated in parallel and independently. These techniques make the SFM more efficient than the SAM model.

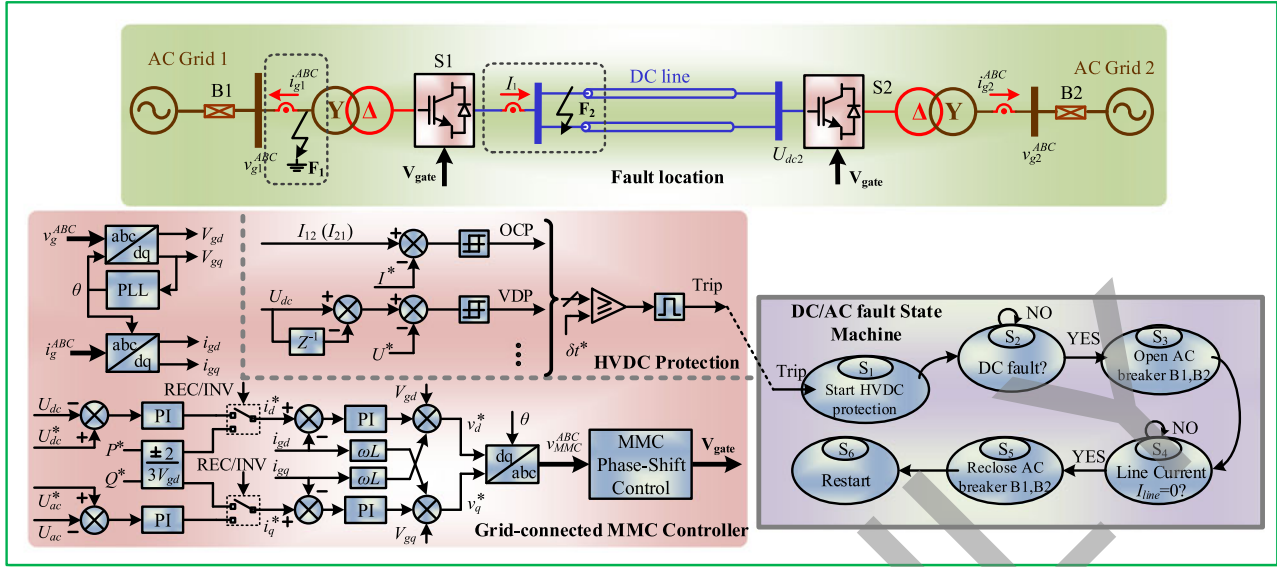


Fig. 6. Two-terminal MMC based HVDC transmissions with half-bridge and full-bridge topologies.

In Fig. 5, both the normal condition and the blocking condition are illustrated. The steady state and the AC fault scenarios of the MMCs can be captured by the equivalent model of the normal condition, while the dc-fault blocking scenario can be simulated by the equivalent model of the blocking condition. When the arm is in the normal condition (condition N), the diode D1 of HBSM is bypassed. Meanwhile, the output voltage of each HBSM can be either positive or zero; thus the diode D2 of HBSM is always off. Different from HBSM, the FBSM preserves two states in the normal condition: positive-inserted or negative-inserted. When the FBSM is positive-inserted, the output voltage will be positive as well, and the reference direction of the equivalent current vector $J_{xy}^F(t)$ is opposite to that of $i_{arm}(t)$; when the FBSM is negative-inserted, the output voltage will be negative, and the reference direction of the equivalent current vector $J_{xy}^F(t)$ is the same as that of $i_{arm}(t)$. When the arm is in the blocking condition (condition B), the diode D1 of the HBSM is free of bypassing, and thus the capacitor of the corresponding HBSM is only allowed to be charged. Unlike the HBSM, the capacitor of the FBSM can be charged according to the direction of $i_{arm}(t)$. When $i_{arm}(t) > 0$, the arm current flows into the sub-module and the sub-module is positive-inserted, and the capacitor of this sub-module will be charged; and when $i_{arm}(t) < 0$, the arm current flows out of the sub-module and the sub-module is negative-inserted, and the value of the capacitor voltage of this sub-module will still rise.

IV. SIMULATION CASE STUDIES

A two-terminal 11-level MMC based HVDC transmissions with half-bridge and full-bridge topologies is considered, which is shown in Fig. 6, to illustrate the advantages of the proposed SFM-based model for MMCs. In this simulation, each arm of the MMC consists of half HBSMs and half FBSMs, and parameters of the MMC are given in Appendix. Station S1 is operated

as the rectifier station while S2 is operated as the inverter station. The AC grid is simplified by using ideal AC sources for the machines. The control schemes of both the rectifier and inverter station are also shown in Fig. 6, where both the control schemes are similar but with different system-level objectives of controllers. Meanwhile, the scheme based on the $d-q$ frame is identical to that of other grid-connected voltage sourced converters (VSCs) except the modulation signals v_{MMC}^{ABC} are sent to an additional MMC inner-loop controller, which, in this case, uses the phase-shift control strategy to generate the driving pulses, i.e., V_{gate} . Regarding the outer control loops: for station S2, the DC voltage control is used to maintain the voltages of DC links, and the reactive power control is used to drive the converter to generate the preset var; for station S1, the converter is controlled to produce target power flows. The DC line protection (LPR) scheme is also covered in Fig. 6. The typical protection schemes for detecting the DC faults include: voltage derivative protection (VDP), under voltage protection (UVP), over current protection (OCP), and current differential protection (CDP). Among these, the two popular protection scheme, OCP and VDP, are utilized. The results of the proposed SFA-based model for MMCs (denoted as ‘‘SFM’’) are compared with the results of the traditional SAMs based on switch function models (denoted as ‘‘SAM’’) [34] and the reference curves. The reference curves are obtained by simulating the whole system under a unanimous time-step of $1 \mu s$.

Moreover, the accuracy of different methods is evaluated by a metric called the relative average simulation error defined as:

$$\epsilon_{avg} = \frac{1}{N} \sum_{i=1}^N \frac{\|x_{num,i} - x_{ref,i}\|}{\|x_{ref,i}\|}, \quad (28)$$

where $x_{num,i}$, $x_{ref,i}$ are the i th sample of monitored variable x in per unit that are produced by different methods; N is the number of samples.

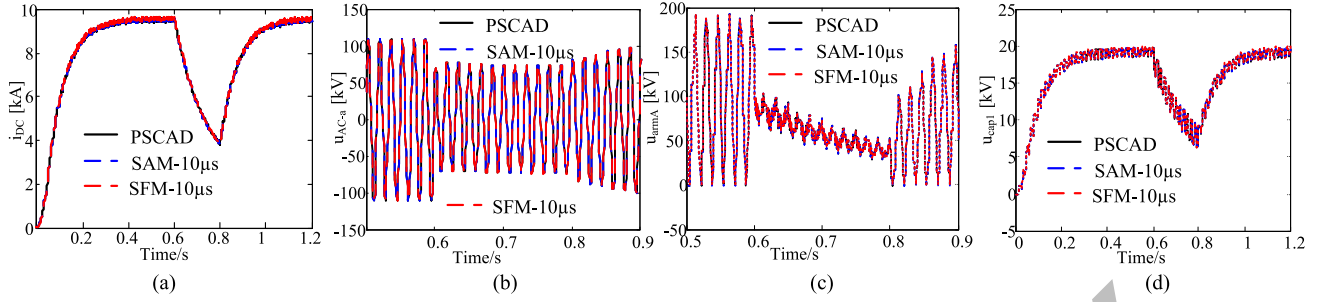


Fig. 7. 300 ms symmetrical AC fault applied at $t = 0.6$ s: (a) DC current; (b) AC voltage of phase-a; (c) upper arm voltage of phase-a; (d) capacitor voltage of sub-module1 in upper arm of phase-a.

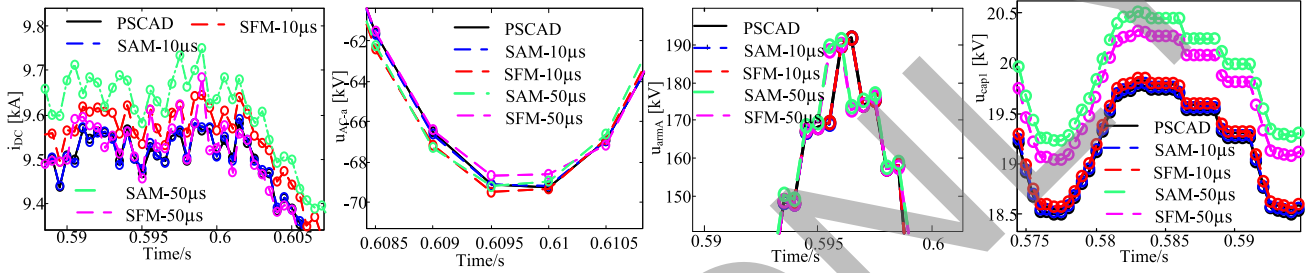


Fig. 8. Enlarged curves of Fig. 7 under different time steps.

TABLE II
ERRORS (ϵ_{avg}) OF DIFFERENT METHODS UNDER DIFFERENT SIMULATION SCENARIOS

Scenario	Methods	v_{g1}^A	u_{dc}	i_{dc}	u_{armA}	i_{armA}	u_{cap} (HBSM)	u_{cap} (FBSM)
AC fault	SAM-10 μ s	0.025	0.005	0.003	0.006	0.003	0.003	0.002
	SAM-50 μ s	0.052	0.028	0.005	0.119	0.103	0.066	0.044
	SFM-10 μ s	0.041	0.005	0.004	0.016	0.075	0.005	0.006
	SFM-50 μ s	0.048	0.012	0.005	0.101	0.025	0.058	0.024
DC fault with blocking	SAM-10 μ s	0.013	0.005	0.005	0.0167	0.004	0.002	0.003
	SAM-50 μ s	0.042	0.002	0.002	0.206	0.010	0.006	0.018
	SFM-10 μ s	0.020	0.005	0.005	0.026	0.006	0.001	0.004
	SFM-50 μ s	0.040	0.001	0.001	0.116	0.009	0.004	0.012

A. Symmetrical AC fault

The first scenario (Fig. 6, F1) is triggered by starting a three-phase resistive fault at the AC bus of station S1 at $t = 0.6$ s. The fault lasts for 300 ms.

As is shown in Fig. 7, both the proposed SFM results and the traditional SAM results match the reference curve very well under the time-step of 10 μ s. However, when the time step is increased to 50 μ s, the SFM results are even more accurate than the SAM results, which is shown in Fig. 8. As shown in Figs. 7(c) and 8(c), both the SFM and the SAM results can capture the switching dynamics of the arm voltage, but the SFM is more accurate. At the time step of 50 μ s, the accuracy of the SFM results has achieved 15% improvement. Moreover, according to Table II, the errors of the DC voltage are reduced from 0.028 pu to 0.012 pu, improving the accuracy of the DC voltage by 58%. This is because the modeling by the SFM is more accurate than that of the SAM, especially for the high-frequency dynamics. The improvement of the arm voltages is due to the accuracy improvement of every sub-module which is

modeled by the SFM, and this impact will result in the accuracy improvement of the output voltage waveforms.

Notably, in Fig. 9, the capacitor voltages of all the sub-modules of upper arm of phase a match very well with the SAM results. Specifically, the capacitor voltages of HBSMs/FBSMs has achieved a 13%/46% improvement of accuracy over those of the SAM model. Therefore, this scenario validates the effectiveness of the SFM of MMC during ac faults, which is primarily focusing on the update of the capacitor voltage of each sub-module.

B. DC Fault Without DC-Fault Blocking

A DC pole-to-pole fault (Fig. 6, F2) is applied at 0.6 s and the controllers of the MMCs are still working, without blocking the IGBTs of each sub-module. In this scenario, the capacitor will be discharged, but due to the role of the diode, the capacitor voltage can only be discharged to zero. Thus, this scenario is specially designed to validate the accuracy of the SFM of the

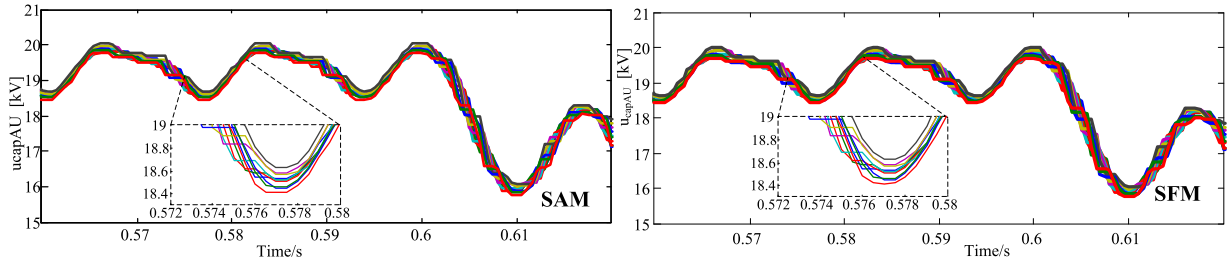


Fig. 9. Capacitor voltages of all the sub-modules in upper arm of phase-a.

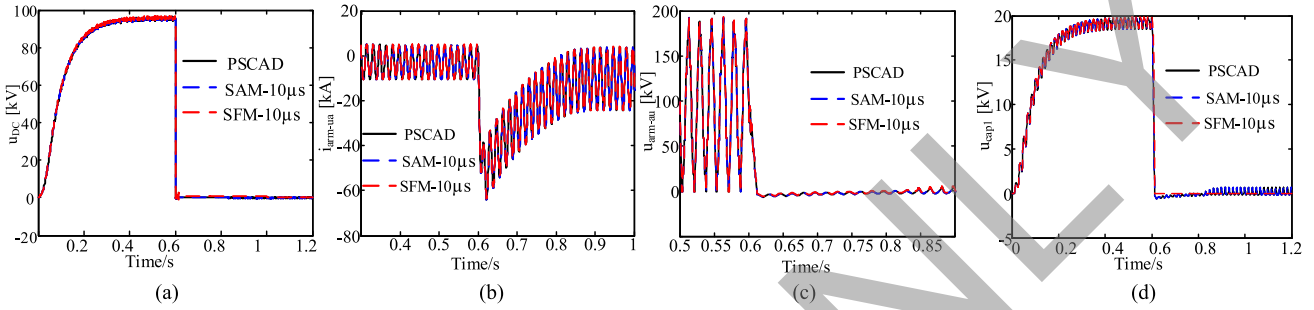
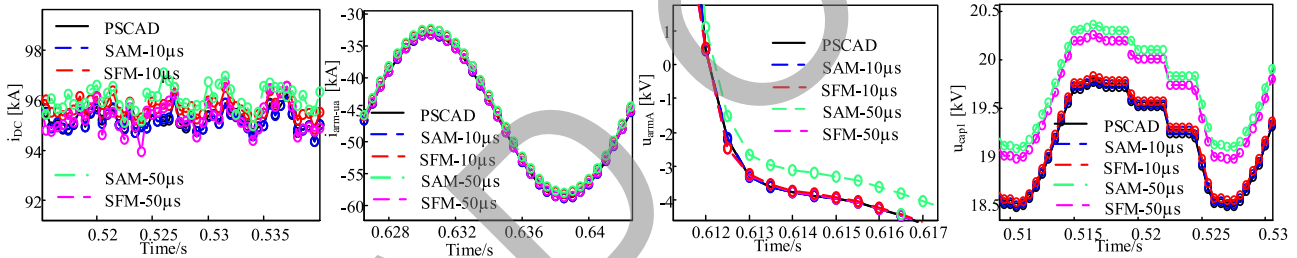
Fig. 10. DC fault applied at $t = 0.6$ s: (a) DC current; (b) arm current of phase-a; (c) upper-arm voltage of phase-a; (d) capacitor voltage of sub-module1 in upper arm of phase-a.

Fig. 11. Enlarged curves of Fig. 10 under different time steps.

MMC when the diode is operated. It should be noted that the diode in the SFM is modeled as a voltage-controlled R_{on}/R_{off} resistance. When the voltage is larger than the forward voltage drop, the diode is on, otherwise, it is in the off condition. The connections between the diode and the Norton equivalent of the arm model are referred to Fig. 5. As shown in Fig. 10, both the SFA results and the SAM results overlap the reference curve. However, when the time-step is increased to $50 \mu\text{s}$, the SFA results are more accurate (see Fig. 11). This observation confirms the effectiveness and numerical consistency of these two models. Moreover, it shows that the SFM results are able to capture the details of fast transients similarly to the SAM results, and the SFM results preserve higher accuracy with increased time-step.

C. DC Fault With DC-Fault Blocking

This scenario is simulated to validate the proposed SFM of the MMC during the blocking condition. A DC pole-to-pole fault is triggered at 0.6 s. When the DC current threshold is reached, the protection schemes block all IGBTs immediately. Thus, the MMC operates in the rectifier mode until at $t = 0.62$ s, the AC circuit breaker (CB) opens to isolate the MMCs. The DC

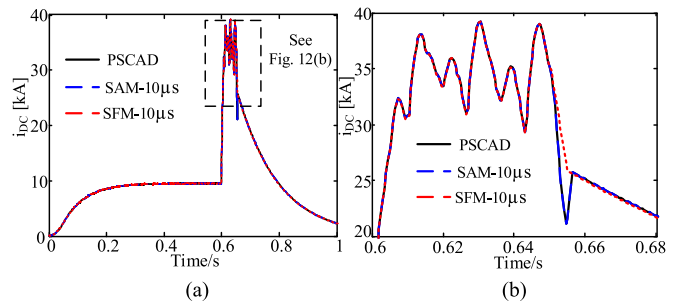


Fig. 12. Curves of DC currents.

currents, as well as capacitor voltages of the HBSM and the FBSM, are shown in Figs. 12 and 13, respectively. All the results match very well when the MMCs are in blocking conditions. As shown in Fig. 13, once the half-bridge sub-module is blocked, its capacitor voltage will remain unchanged. This is because the capacitor of the HBSM will not be charged when the DC voltage is higher than the AC voltage of the other side. On the contrary, even if the full-bridge sub-module is blocked, the capacitor of the HBSM can still be charged. According to

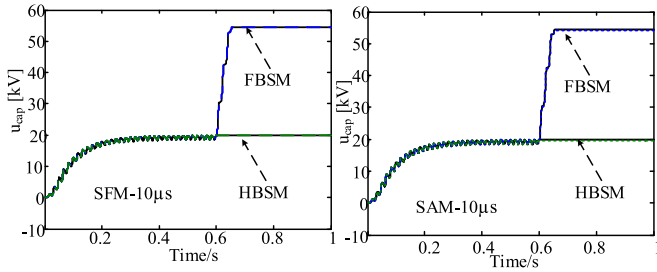


Fig. 13. Curves of capacitor voltages of the HBSM and the FBSM.

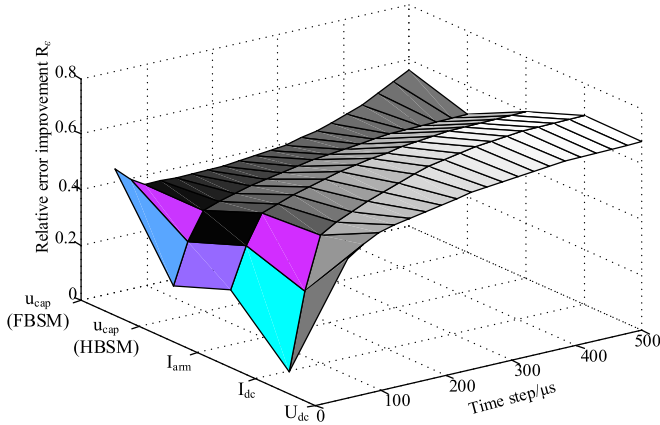


Fig. 14. Accuracy improvement of SFM compared with SAM.

the analysis in Section III-B, when $i_{arm}(t) < 0$ and the FBSM is negative-inserted, the current is flowing from the AC side to the fault location on the DC side. All the FBSMs in the arm provide negative capacitor voltages in the circuit loop, which can help to limit the DC fault current. At the same time, the absolute values of capacitor voltages of the FBSMs will increase. When $i_{arm}(t) > 0$, all the FBSMs are positive-inserted; therefore, both HBSMs and FBSMs provide positive voltages against the AC voltage of the other side, aiming to limit the DC fault current. In this scenario, capacitor voltages of all the FBSMs are still being charged, which is shown in Fig. 13. Only when the circuit breaker of the AC side is open, the DC current gradually drops to zero, and the capacitor voltages of all the FBSMs remain unchanged.

According to Table II, when the time step is $50 \mu s$, the DC voltage achieves an improved accuracy by 50%. Capacitor voltages of HBSM/FBSM all have a 33.3% improved accuracy. The relative accuracy improvement of SFM compared to the traditional SAM, i.e., $R_\epsilon = \frac{|\epsilon_{avg}^{SAM} - \epsilon_{avg}^{SFM}|}{\epsilon_{avg}^{SAM}}$ is shown in Fig. 14, where ϵ_{avg}^{SAM} , ϵ_{avg}^{SFM} are the average simulation errors of SAM/SFM, respectively. Fig. 14 shows that the improvement of accuracy as the time step rises. Specifically, the DC quantities, i.e., the DC current and the DC voltage, achieve a more than 50% improvement of accuracy when the time step is increased to $200 \mu s$. When the time step is larger, the accuracy of both the SFM model and the SAM model will become worse. However, Fig. 14 illustrates that when the time step is larger, the accuracy improvement of SFM model over the SAM model is more significant.

TABLE III
COMPARISONS OF EXECUTION TIME UNDER DIFFERENT TIME STEPS (UNIT:S)

Levels	Ref.	SAM- 50 μs	Acceleration ratio	SFM- 50 μs	Acceleration ratio
11	31.2	4.3	7.2	2.3	13.6
21	97.8	6.5	15.0	3.2	30.6
51	1257.6	14.2	88.5	5.7	220.6
101	8299.8	22.3	370.5	11.9	697.5
401	39627.1	80.7	491	40.7	973.6

D. Comparison of Accuracy and Computational Performance

Table II lists the average errors of different methods during various simulation scenarios. As can be seen, the SFM results are as accurate as the SAM results, both below 0.05 pu. However, when the time-step is increased to $50 \mu s$, the SFM results are more accurate. In addition, the total CPU time are compared in Table III, where the simulation period for the case is 1.2 s. All simulation results are carried out on a 2.67 GHz Intel i7 CPU; with 8 GB of RAM and a 64-b Windows 7 operating system. It should be noted that except the modeling approach, all the conditions are set the same for both the proposed SFM model and the SAM model. Especially, both these two models adopt the parallel computing environment, i.e., C++ coding using openMP, to update capacitor voltages by multicore CPU with 8 cores. It is shown that the SFM results are more efficient than the SAM results under the same step. When the level of the MMC is 401, the simulation time is reduced from 39627.1 s to 40.7 s, more than 900 times faster than the reference results. The proposed SFM results achieve an improvement of 98% compared with the SAM results. Notably, as the level of the MMC increases, the improvement of efficiency is more significant. The reason why the proposed SFM can achieve such improvement of efficiency is because this model is actually a two-stage model. The first stage is to solve the global node voltage equation, where each arm of the MMC is represented by one Norton equivalent circuit. The number of nodes will not expand as the number of sub-modules increases, and only one node will be added in the node voltage equations. This node is the connecting node between upper and lower arms. In the second stage, the capacitor voltages are refreshed in a parallel and independent way according to (17), which, taking the real and imaginary parts into account, is only a two-dimensional equation and thus can be very efficiently worked out. Considering its accuracy and computational performances, the proposed model is expected to be more suitable for simulating large-scale DC grids.

V. CONCLUSION

In this paper, the shifted frequency modeling (SFM) of the half- and full-bridge MMC is proposed to improve the accuracy and efficiency of simulations of MMC-based DC grids. One of its salient features is that the SFM of the MMC has improved accuracy than SAMs as each sub-module inside an arm is modeled by dynamic phasor based Thévenin equivalents. The other important feature is that the arm model of the half-bridge and full-bridge MMC is represented by Norton equivalents, consid-

ering both normal and dc-blocking conditions, to guarantee the efficiency.

The effectiveness of the proposed method has been validated by simulation studies of a MMC based HVDC transmission. Compared with the traditional SAMs, the proposed SFM can reduce the simulation execution time significantly. Moreover, Its calculation errors are limited below 0.04 pu at the time-step of 10 μ s, and it is even more accurate than the traditional models when the time step is increased. Future applications of the proposed model include real-time simulations of large-scale DC grids.

APPENDIX A SHIFTED FREQUENCY MODELING BASED ON PARK TRANSFORMATION

Given the equation satisfying:

$$\frac{de}{dt} = F(u) = Ku, \quad (29)$$

where u is the input, e is the output; K is the gain. Equation (29) is rewritten with their dynamic phasors [27], [28]:

$$\frac{d}{dt} \begin{bmatrix} e_I \\ e_Q \end{bmatrix} = KI_{2 \times 2} \begin{bmatrix} u_I \\ u_Q \end{bmatrix} - W \begin{bmatrix} e_I \\ e_Q \end{bmatrix}, \quad (30)$$

where

$$W = \omega_s \begin{bmatrix} 1 & 0 \\ 0 & -1 \end{bmatrix}, \quad (31)$$

Adopting the trapezoidal algorithm, (30) is discretized as:

$$\begin{aligned} \left(\frac{2}{\Delta t} I_{2 \times 2} + W \right) \begin{bmatrix} e_I(t) \\ e_Q(t) \end{bmatrix} &= \left(\frac{2}{\Delta t} I_{2 \times 2} - W \right) \begin{bmatrix} e_I(t - \Delta t) \\ e_Q(t - \Delta t) \end{bmatrix} \\ &+ K \begin{bmatrix} u_I(t) \\ u_Q(t) \end{bmatrix} + K \begin{bmatrix} u_I(t - \Delta t) \\ u_Q(t - \Delta t) \end{bmatrix}, \end{aligned} \quad (32)$$

The dynamic phasor is transformed into time domain signal by means of Park transform [35]:

$$\begin{bmatrix} e_x \\ e_y \end{bmatrix} = \begin{bmatrix} \cos \omega_s t & \sin \omega_s t \\ -\sin \omega_s t & \cos \omega_s t \end{bmatrix} \begin{bmatrix} e_I \\ e_Q \end{bmatrix} = \mathbf{R}(t) \begin{bmatrix} e_I \\ e_Q \end{bmatrix}, \quad (33)$$

Therefore, the final discretized equation for (32) is formulated as:

$$\begin{aligned} \left(\frac{2}{\Delta t} I_{2 \times 2} + W \right) \begin{bmatrix} e_x(t) \\ e_y(t) \end{bmatrix} &= \left(\frac{2}{\Delta t} I_{2 \times 2} - W \right) \mathbf{R}(-\Delta t) \\ &\begin{bmatrix} e_x(t - \Delta t) \\ e_y(t - \Delta t) \end{bmatrix} + K \begin{bmatrix} u_x(t) \\ u_y(t) \end{bmatrix} + K \mathbf{R}(-\Delta t) \begin{bmatrix} u_x(t - \Delta t) \\ u_y(t - \Delta t) \end{bmatrix}, \end{aligned} \quad (34)$$

APPENDIX B PARAMETERS OF THE MTDC GRIDS

The MTDC system parameters are: frequency f_s : 60 Hz; angular velocity ω_s : 120 π rad/s; AC voltage: 110 kV,

Transformers: 110 kV/230 kV, capacitor of each sub-module : 1200 μ F, arm inductance: 15 mH, DC power: 1000 MW, DC link voltage: 100 kV; DC line: impedance $r_0 = 0.012 \Omega/\text{km}$, inductance $l_0 = 0.106 \text{ mH/km}$, capacitance $c_0 = 0.296 \mu\text{F/km}$, length $D = 200 \text{ km}$.

Control Parameters: outer loop controllers of constant DC voltage: $K_p = 2, K_I = 0.0025$; outer loop controllers of constant reactive power: $K_p = 0.001, K_I = 0.15$; the phase shift loop: $K_p = 0.5, K_I = 150$.

REFERENCES

- [1] A. Lesnicar and R. Marquardt, "An innovative modular multilevel converter topology suitable for a wide power range," in *Proc. IEEE Bologna Power Tech Conf.*, Bologna, Italy, 2003, vol. 3, pp. 23–26.
- [2] M. H. Rahman, L. Xu, and L. Yao, "Protection of large partitioned MTDC networks using DC-DC converters and circuit breakers," *Protection Control Mod. Power Syst.*, vol. 1, no. 1, pp. 1–9, Dec. 2016.
- [3] Z. Shen and V. Dinavahi, "Real-time device-level transient electrothermal model for modular multilevel converter on FPGA," *IEEE Trans. Power Electron.*, vol. 31, no. 9, pp. 6155–6168, Sep. 2016.
- [4] T. Liang, and V. Dinavahi, "Real-time system-on-chip emulation of electro-thermal models for power electronic devices via Hammerstein configuration," *IEEE J. Emerg. Sel. Topics Power Electron.*, vol. PP, no. 99, 2017.
- [5] U. N. Gnanarathna, A. M. Gole, and R. P. Jayasinghe, "Efficient modeling of modular multilevel HVDC converters (MMC) on electromagnetic transient simulation programs," *IEEE Trans. Power Del.*, vol. 26, no. 1, pp. 316–324, Jan. 2011.
- [6] W. Xiang, W. Lin, T. An, J. Wen, and Y. Wu, "Equivalent electromagnetic transient simulation model and fast recovery control of overhead VSC-HVDC based on SB-MMC," *IEEE Trans. Power Del.*, vol. 32, no. 2, pp. 778–788, Apr. 2017.
- [7] Q. Song, W. Liu, X. Li, H. Rao, S. Xu, and L. Li, "A Steady-state analysis method for a modular multilevel converter," *IEEE Trans. Power Electron.*, vol. 28, no. 8, pp. 3702–3713, Aug. 2013.
- [8] L. Harnefors, A. Antonopoulos, S. Norrga, L. Angquist and H. P. Nee, "Dynamic analysis of modular multilevel converters," *IEEE Trans. Ind. Electron.*, vol. 60, no. 7, pp. 2526–2537, Jul. 2013.
- [9] D. Jovicic and A. Jamshidifar, "Phasor model of modular multilevel converter with circulating current suppression control," *IEEE Trans. Power Del.*, vol. 30, no. 4, pp. 1889–1897, Aug. 2015.
- [10] H. Saad *et al.*, "Modular multilevel converter models for electromagnetic transients," *IEEE Trans. Power Del.*, vol. 29, no. 3, pp. 1481–1489, Jun. 2014.
- [11] S. S. Khan, J. A. Suul, E. Tedeschi, and M. Jafar, "Blocking capability for switching function and average models of modular multilevel converters," in *Proc. IEEE 16th Int. Conf. Environ. Elect. Eng.*, Florence, Italy, 2016, pp. 1–6.
- [12] D. Shu *et al.*, "A two-stage efficient model of modular multilevel converter for electromagnetic transient simulation," in *Proc. 18th Eur. Conf. Power Electron. Appl.*, 2016, pp. 1–10.
- [13] H. Yang, Y. Dong, W. Li, and X. He, "Average-value model of modular multilevel converters considering capacitor voltage ripple," *IEEE Trans. Power Del.*, vol. 32, no. 2, pp. 723–732, Apr. 2017.
- [14] J. Xu, C. Zhao, W. Liu, and C. Guo, "Accelerated model of modular multilevel converters in PSCAD/EMTDC," *IEEE Trans. Power Del.*, vol. 28, no. 1, pp. 129–136, Jan. 2013.
- [15] D. Shu *et al.*, "A multirate EMT co-simulation of large AC and MMC-based MTDC systems," *IEEE Trans. Power Sys.*, vol. PP, no. 99, 2017.
- [16] S. Deore, P. Darji, and A. Kulkarni, "Dynamic phasor modeling of modular multi-level converters," in *Proc. IEEE 7th Int. Conf. Ind. Inf. Syst.*, 2012, pp. 1–6.
- [17] S. Rajesvaran and S. Filizadeh, "Modeling modular multilevel converters using extended-frequency dynamic phasors," in *Proc. IEEE Power Energy Soc. Gen. Meeting*, 2016, pp. 1–5.
- [18] J. Peralta, H. Saad, S. Denneriere, J. Mahseredjian, and S. Nguefeu, "Detailed and averaged models for a 401-Level MMC–HVDC system," *IEEE Trans. Power Del.*, vol. 27, no. 3, pp. 1501–1508, Jul. 2012.
- [19] S. R. Sanders, "On limit cycles and the describing function method in periodically switched circuits," *IEEE Trans. Circuits Syst. I*, vol. 40, no. 40, pp. 564–572, Sep. 1993.

- [20] S. R. Sanders, J. M. Noworolski, X. Z. Liu, and G. C. Verghese, "Generalized averaging method for power conversion circuits," *IEEE Trans. Power Electron.*, vol. 6, no. 2, pp. 251–259, Apr. 1991.
- [21] P. Zhang, J. R. Marti, and H. W. Dommel, "Synchronous machine modelling based on shifted frequency analysis," *IEEE Trans. Power Syst.*, vol. 22, no. 3, pp. 1139–1147, Aug. 2007.
- [22] P. Zhang, J. R. Marti, and H. W. Dommel, "Induction machine modelling based on shifted frequency analysis," *IEEE Trans. Power Syst.*, vol. 24, no. 1, pp. 157–164, Feb. 2009.
- [23] M. Elizondo, F. Tuffner, and K. Schneider, "Simulation of inrush dynamics for unbalanced distribution systems using dynamic-phasor models," *IEEE Trans. Power Syst.*, vol. 32, no. 1, pp. 633–642, Jan. 2017.
- [24] P. Zhang, J. R. Marti, and H. Dommel, "Shifted-frequency analysis for EMT simulation of power-system dynamics," *IEEE Trans. Circuits Syst. I, Reg. Papers*, vol. 57, no. 9, pp. 2564–2574, Sep. 2010.
- [25] L. Cohen, *Time-Frequency Analysis.*, Englewood Cliffs, NY, USA: Prentice-Hall, 1995.
- [26] Y. Huang, M. Chaparaha, F. Therrien, J. Jatskevich, and J. R. Marti, "A constant-parameter voltage-behind-reactance synchronous machine model based on shifted-frequency analysis," *IEEE Trans. Energy Convers.*, vol. 30, no. 2, pp. 761–771, Jun. 2015.
- [27] K. Strunz, R. Shintaku, and F. Gao, "Frequency-adaptive network modeling for integrative simulation of natural and envelope waveforms in power systems and circuits," *IEEE Trans. Circuits Systems I, Reg. Papers*, vol. 53, no. 12, pp. 2788–2803, Dec. 2006.
- [28] F. Gao and K. Strunz, "Frequency-adaptive power system modeling for multi-scale simulation of transients," *IEEE Trans. Power Syst.*, vol. 24, no. 2, pp. 561–571, May 2009.
- [29] J. A. Martinez-Velasco, *Transient Analysis of Power Systems: Solution Techniques, Tools and Applications.* Piscataway, NJ, USA: Wiley, 2015.
- [30] D. Shu, X. Xie, S. Zhang, and Q. Jiang, "Hybrid method for numerical oscillation suppression based on rational-fraction approximations to exponential functions," *IET Gener., Transm. Distrib.*, vol. 10, no. 11, pp. 2825–2832, Aug. 2016.
- [31] H. W. Dommel, "Digital computation of electromagnetic transients in single and multi-phase networks," *IEEE Trans. Power App. Syst.*, vol. PAS-88, no. 4, pp. 388–399, Apr. 1969.
- [32] H. W. Dommel, *EMTP Theory Book.* Portland, OR, USA: Bonneville Power Admin., Aug. 1986.
- [33] Y. Hua, and K. Strunz, "Multi-scale and frequency-dependent modeling of electric power transmission lines," *IEEE Trans. Power Del.*, vol. PP, no. 99, 2017.
- [34] K. Sharifabadi, L. Harnefors, H.-P. Nee, S. Norrga, and R. Teodorescu, *Design, Control and Application of Modular Multilevel Converters for HVDC Transmission Systems.* New York, NY, USA: Wiley, 2016, ch. 6, pp. 278–281.
- [35] S. Fan and H. Ding, "Time domain transformation method for accelerating EMT simulation of power system dynamics," *IEEE Trans. Power Syst.*, vol. 27, no. 4, pp. 1778–1787, Nov. 2012.



Dewu Shu (S'14) received the B.Sc. degree in electrical engineering from Tsinghua University, Beijing, China, in 2013. He is currently working toward the Ph.D. degree in the Department of Electrical Engineering, Tsinghua University. In 2017, he was a Visiting Scholar in RTX Lab, University of Alberta, Edmonton, AB, Canada. His research interests include multirate EMT/TLS simulations, and parallel and distributed computing.



Venkata Dinavahi (SM'08) received the Ph.D. degree from the University of Toronto, Toronto, ON, Canada, in 2000. He is currently a Professor in the Department of Electrical and Computer Engineering, University of Alberta, Edmonton, AB, Canada. His research interests include real-time simulation of power systems and power electronic systems, large-scale system simulation, and parallel and distributed computing.



Xiaorong Xie received the B.Sc. degree from Shanghai Jiao Tong University, Shanghai, China, and the Ph.D./M.Eng. degrees from Tsinghua University, Beijing, China, in 1996 and 2001, respectively. From 2001 to 2005, he was a Lecturer in the Department of Electrical Engineering, Tsinghua University, where he has been an Associate Professor since 2005. His research interests include power system analysis and control, and flexible ac transmission systems.



Qirong Jiang (M'98) received the B.S. and Ph.D. degrees in electrical engineering from Tsinghua University, Beijing, China, in 1992 and 1997, respectively. Since 2006, he has been a Professor at Tsinghua University. His research interests include power system analysis and control, modeling and control of flexible ac transmission systems, power quality analysis and mitigation, power electronic equipment, and renewable energy power conversion.